ELSEVIER

Contents lists available at ScienceDirect

Materials Science & Engineering A

journal homepage: http://www.elsevier.com/locate/msea





Structural and microstructural influence on deformation and fracture of dual-phase steels

Xinzhu Zheng^a, Hassan Ghassemi-Armaki^b, Ankit Srivastava^{a,*}

- ^a Department of Materials Science & Engineering, Texas A&M University, College Station, TX, USA
- ^b ArcelorMittal Global R&D East Chicago, East Chicago, IN, USA

ARTICLE INFO

Keywords:
Characterization
Finite element analysis
In situ tension test
Digital image correlation
Plasticity
Fracture behavior

ABSTRACT

The objective of this work is to demonstrate that the mechanical response of multiphase materials is fundamentally different in an imposed deformation field that is homogeneous, versus in an imposed deformation field that is heterogeneous, at a length-scale greater than the microstructural length-scale. To this end, we focus on two dual-phase steels with significantly different nominal chemical composition and microstructure. The mechanical response of the steels is characterized by in-situ SEM tensile tests of flat dog-bone and single-edge notch specimens. The experimental results show that the dog-bone specimens of the two steels exhibit very similar mechanical response but the mechanical response of their single-edge notch specimens differs significantly. This is in contrast to any classical analysis that will predict the same mechanical response in the presence of a notch for two materials that give the same mechanical response under uniaxial tension. The high resolution in-situ tests coupled with microstructure-based digital image correlation and finite element analysis are then used to elucidate how the interlacing of imposed heterogeneous deformation field and material microstructure affects the mechanical response of these steels. Our results clearly highlight that a mechanistic analysis of multiphase materials under imposed heterogeneous deformation field must involve explicit consideration of the length-scales associated with the material microstructure.

1. Introduction

Materials science of structural materials seeks the forward correlation of composition/processing, material microstructure and a set of mechanical properties. This forward correlation is likely unique i.e. a fixed composition/processing route leads to a unique microstructure that in turn leads to a unique set of mechanical properties. Intuitively, the inverse correlation of the same is not necessarily unique i.e. the same set of mechanical properties can be obtained from more than one microstructure resulting from different composition/processing routes. The key phrase here is "a set of mechanical properties." In general, mechanical properties of a ductile structural material are characterized via the standard tension test [1]. In the tension test, the gauge section of the test specimen undergoes homogeneous uniaxial tensile deformation at a length-scale greater than the microstructural length-scale at least until the onset of necking [2]. Thus, as long as the specimen size i.e. the structural length-scale is sufficiently greater than the microstructural length-scale, an unstructured continuum description of (a set of) mechanical properties can be obtained. These mechanical property

descriptors are then be used for comparing materials, material development, structure/component design, quality control and reliability analysis, to name a few.

There is, however, an important difference between the characterization of mechanical response of a structural material in a deformation field that is homogeneous, versus in a deformation field that is heterogeneous at the structural length-scale, such as those observed in bending dominated manufacturing processes or in the vicinity of a structural discontinuity. In the former, characterization of mechanical response can be based on an unstructured continuum description of mechanical properties, such as strength and strain-hardening. On the contrary, in the latter, the characterization of mechanical response may also involve the length-scales associated with the material microstructure. This implies that even if the mechanical response of more than one microstructure is the same in a homogeneous deformation field, for example, under a tension test, it may still differ in a heterogeneous deformation field, for example, in the presence of a notch. This has far reaching consequences in materials selection, development and their use in critical applications.

^{*} Corresponding author. Department of Materials Science and Engineering, 3003 TAMU, College Station, TX, 77843, USA. *E-mail address:* ankit.sri@tamu.edu (A. Srivastava).

The objective of this work is to experimentally demonstrate that two microstructures that lead to the same mechanical response in a homogeneous deformation field can lead to very different mechanical response in a heterogeneous deformation field. To this end, we focus on two low-carbon dual-phase [3] advanced high strength steels [4], viz, DF140T and DP980, with significantly different nominal chemical compositions. Both of these steels were produced on a continuous annealing line that allows intercritical heating into the ferrite-austenite phase field followed by fast cooling to cause diffusionless martensitic transformation. The as-processed microstructure of both dual-phase steels consists of hard martensite phase particles dispersed in relatively soft ferrite phase matrix. However, the amount of ferrite and martensite phases, and their mechanical properties, such as strength and strain-hardening, in the as-processed microstructure of these two steels differ significantly [5–7].

Dual-phase advanced high strength steels are one of the most technologically sought after materials to enhance safety and efficiency of automobiles [8]. The microstructure – mechanical property correlation of dual-phase steels has been a topic of several experimental and computational studies [5–7,9–40]. These studies have shown that under uniaxial tension, the stress-strain curves of dual-phase steels (with high martensite content) exhibit three characteristic stages: (i) at low loads the response is elastic and with increasing load yielding first occurs in the soft ferrite phase; (ii) following yielding in the ferrite phase, a period of rather strong strain-hardening is observed where the hard martensite phase remains elastic; and (iii) with further increase in load the martensite phase also reaches yield resulting in a significant reduction in the strain-hardening rate. These studies have also shown that dual-phase steels predominantly undergo ductile fracture at room temperature due to nucleation, growth and coalescence of voids, where void nucleation predominantly occurs by decohesion at ferrite - martensite interfaces and separation of adjacent or fractured martensite particles.

Here, we carry out a series of in-situ SEM tensile tests of flat dog-bone and single-edge notch specimens of DF140T and DP980 dual-phase advanced high strength steels. The tensile test of a dog-bone specimen corresponds to an imposed homogeneous deformation field (at least until the onset of necking) whereas that of a single-edge notch specimen corresponds to an imposed heterogeneous deformation field at the structural length-scale. The high resolution in-situ SEM tensile tests coupled with microstructure-based digital image correlation [12,13,24, 25,27] allow us to capture both the macroscopic mechanical response and the distribution of microscale strains on the specimen surface. Our experimental results show that despite significantly different microstructure, microscale property distribution and microscale deformation, the dog-bone specimens of the two steels exhibit very similar mechanical response at macroscale. However, the mechanical response of the single-edge notch specimens of the two steels differs significantly.

Our microscale strain measurements (prior to the onset of necking/fracture) coupled with fractographic analyses suggest that the interlacing of heterogeneous deformation field at the structural and the microstructural length-scales affects the deformation and fracture response of dual-phase steels. We also carry out microstructure-based finite element analyses of tensile tests of flat dog-bone and single-edge notch specimens of both the steels to complement the conclusions drawn from the experimental observations. In the finite element calculations, the SEM images of the microstructures of the steels under consideration are directly utilized to generate two-dimensional finite element meshes and the constitutive properties of the constituent phases are obtained from the micropillar compression test and finite element calculation results of refs. [5–7].

2. Material and method

The dual-phase advanced high strength steels examined in this work are DF140T with nominal chemical composition of 0.15%C-1.45%Mn-0.3%Si (wt.%) and DP980 with nominal chemical composition of

0.09%C-2.15%Mn-0.6%Si (wt.%). Both of these steels were produced on a water – quenched continuous anneal line by ArcelorMittal. The deformation and fracture response of both the steels were characterized using tensile tests inside a Scanning Electron Microscope (SEM). The metallographic analysis of the undeformed material and fractography of the fractured specimens were also carried out using SEM.

The in-situ SEM tensile tests were carried out using a Kammrath & Weiss tension module inside a Tescan FERA-3 model GMH Focused Ion Beam Microscope. For in-situ SEM tensile tests, sub-sized flat dog-bone and single-edge notch tension specimens with axis parallel to the rolling direction of the steel sheets were machined using wire EDM. The length and width of the gauge section of the dog-bone specimens were 8 mm and 3 mm, respectively. The single-edge notch specimens had the same dimensions as the dog-bone specimens but they contained an edge notch of depth 1.5 mm, machined using wire EDM in the center of the gauge section. The final tip radii of EDM machined notches were approximately 150 μm . Prior to in-situ SEM tensile testing, one surface of all the flat tension specimens was mechanically ground using 320 to 1200 grit SiC grinding papers and fine polished until 0.05 μm alumina suspension. All the mechanically polished specimens were chemically etched with 3% Nital for 15sec to reveal the dual-phase microstructure. The final thickness of the polished and etched tension specimens was approximately 1.35 mm. All the tension tests were carried out at a crosshead speed of 4 µm/s giving a nominal uniaxial tensile strain rate of $0.5 \times 10^{-3} \text{sec}^{-1}$ for the dog-bone specimens.

The in-situ SEM tensile tests were interrupted at regular intervals to capture high resolution secondary electron (SE) images of the surface microstructure. The series of SE images of the surface microstructure captured during a tensile test were then used to carry out microstructure-based digital image correlation (DIC) by tracking the contrast between the microstructural features. The DIC analyses were performed using the Ncorr open-source DIC software [41]. The Ncorr software utilizes a subset-based DIC algorithm, where the reference image is partitioned into smaller regions referred to as subsets. The subsets are initially a contiguous circular group of points. In this work, subsets of radii 35 pixels with inter subset spacing of 1 pixel were used. The Ncorr software utilizes the inverse compositional method [42] for two-dimensional displacement field measurements, where the subsets in the current image are mapped with the subsets in the reference image via linear displacement mapping functions. The measured displacement fields were then used to estimate Green-Lagrange strain. The Green-Lagrange strain contains the derivatives of the displacement with respect to the initial configuration, and represents the strains in the material orientation instead of the spatial orientation.

3. Experimental results

3.1. Material microstructure and macroscale mechanical response

The SE-SEM images of the mechanically polished and chemically etched specimens of undeformed DF140T and DP980 steels are shown in Figs. 1(a) and (b), respectively. The microstructure of both the steels consists of islands of hard martensite particles dispersed in a matrix of relatively soft ferrite grains. The microstructure of DF140T is composed of ${\sim}39~\pm~2\%$ martensite and rest ferrite, while that of DP980 is composed of ${\sim}61 \pm 3\%$ martensite and rest ferrite. The descending cumulative distribution function (CDF) curves of the size of ferrite and martensite regions in both the steels are shown in Fig. 1(c). The CDF curves can be interpreted as displaying the probability that the size of a feature will exceed a given value on the horizontal axis. From Fig. 1(c), it is clear that the probability that the size of ferrite region will exceed a given threshold is greater in DF140T, whereas the probability that the size of martensite region will exceed a given threshold is greater in DP980. If we ignore the smallest 5% and largest 5% feature sizes, in DF140T the size of ferrite region lies within 1.83–11.32 μm and the size

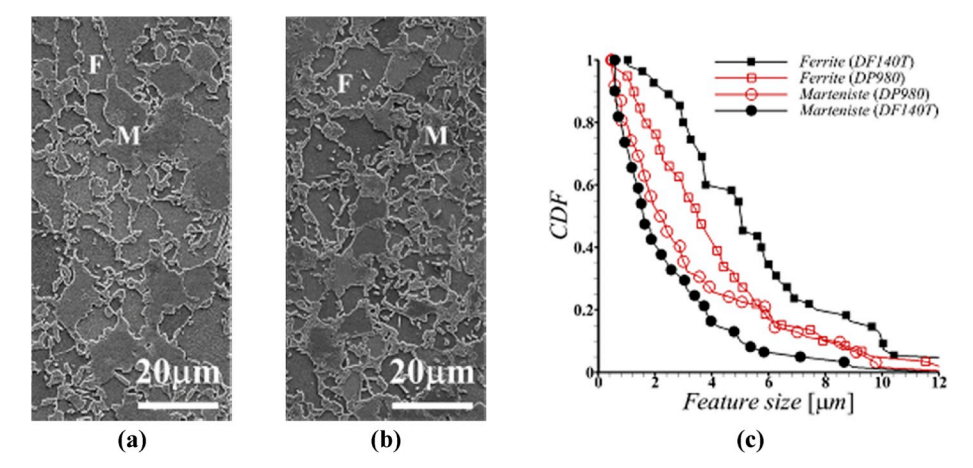


Fig. 1. SE-SEM images of initial microstructures of (a) DF140T and (b) DP980 dual-phase (ferrite (F) and martensite (M)) advanced high strength steels. (c) The descending cumulative distribution function (CDF) of the size of ferrite and marteniste regions in the initial microstructure of DF140T and DP980 dual-phase advanced high strength steels.

of martensite region lies within 0.59–7.15 $\mu m.$ Similarly, in DP980 the size of ferrite region lies within 1.05–9.60 μm and the size of martensite region lies within 0.52–9.44 $\mu m.$ So that, on average the size of ferrite region is greater in DF140T compared to DP980, whereas the size of martensite region is greater in DP980 compared to DF140T.

The load-displacement curves of flat dog-bone and single-edge notch specimens of DF140T and DP980 steels under tension are shown in Figs. 2(a) and (b), respectively. All the tensile tests were carried out inside an SEM and the tests were interrupted at regular intervals to capture SE images of the evolving surface microstructure. The small drops in load at regular displacement intervals in Fig. 2 mark the interruption of tensile loading. As shown in Fig. 2(a), the tensile response of the dog-bone specimens of both the steels is very similar with ultimate tensile strength i.e. maximum load (~4300 N) normalized by the initial cross-section area of the gauge section of the dog-bone specimens of both the steels being ~1 GPa. However, the tensile response of single-edge notch specimens of the two steels differs significantly, Fig. 2(b). The single-edge notch specimens of DP980 steel can withstand greater than 6% load and exhibit more than 60% greater extension prior to fracture as compared to the single-edge notch specimens of DF140T steel. Note that for two materials with very similar mechanical response under uniaxial tension, any classical fracture mechanics-based analysis will predict similar response in the presence of a structural defect such as a notch. The results presented in Fig. 2 clearly highlight the difference between the characterization of mechanical response of multiphase materials in an imposed deformation field that is homogeneous, versus in an imposed deformation field that is heterogeneous at the structural length-scale.

3.2. Microscale deformation field

A series of SE-SEM images of the evolving microstructure on the surface of the flat tension specimen were captured to characterize the inplane microscale deformation field via microstructure-based DIC. The distribution of the ε_{xx} strain (strain along the tensile loading direction) in the reference configuration in a 300-by-300 μ m² region in the center of the gauge section of the dog-bone tension specimen of DF140T and DP980 steels deformed to a (macroscale) displacement of 600 μ m is shown in Fig. 3(a). At this point, the dog-bone tension specimens of both the steels are within the uniform deformation regime, see Fig. 2(a). In Fig. 3(a), the values of ε_{xx} less than the value of ε_{xx} at the edges parallel to *y*-axis of the 300-by-300 μ m² box, ε_{xx}^{box} , are white washed to highlight the regions of strain concentration. As shown in the figure, even though the dog-bone tension specimens of both the steels at macroscale are within uniform deformation regime, at microscale the deformation is extremely heterogeneous. Also, even though at macroscale the

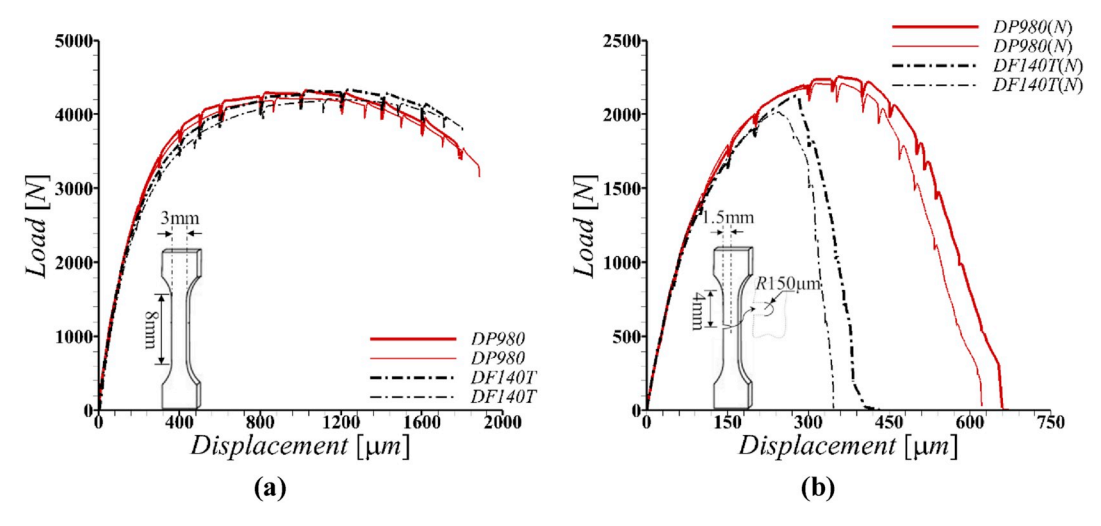


Fig. 2. Two sets of load-displacement curves of flat (a) dog-bone and (b) single-edge notch tension specimens of DF140T and DP980 dual-phase advanced high strength steels. The small drops in load at regular displacement intervals are caused by interrupting the test to capture high resolution SE-SEM images of the evolving microstructure on the specimen surface.

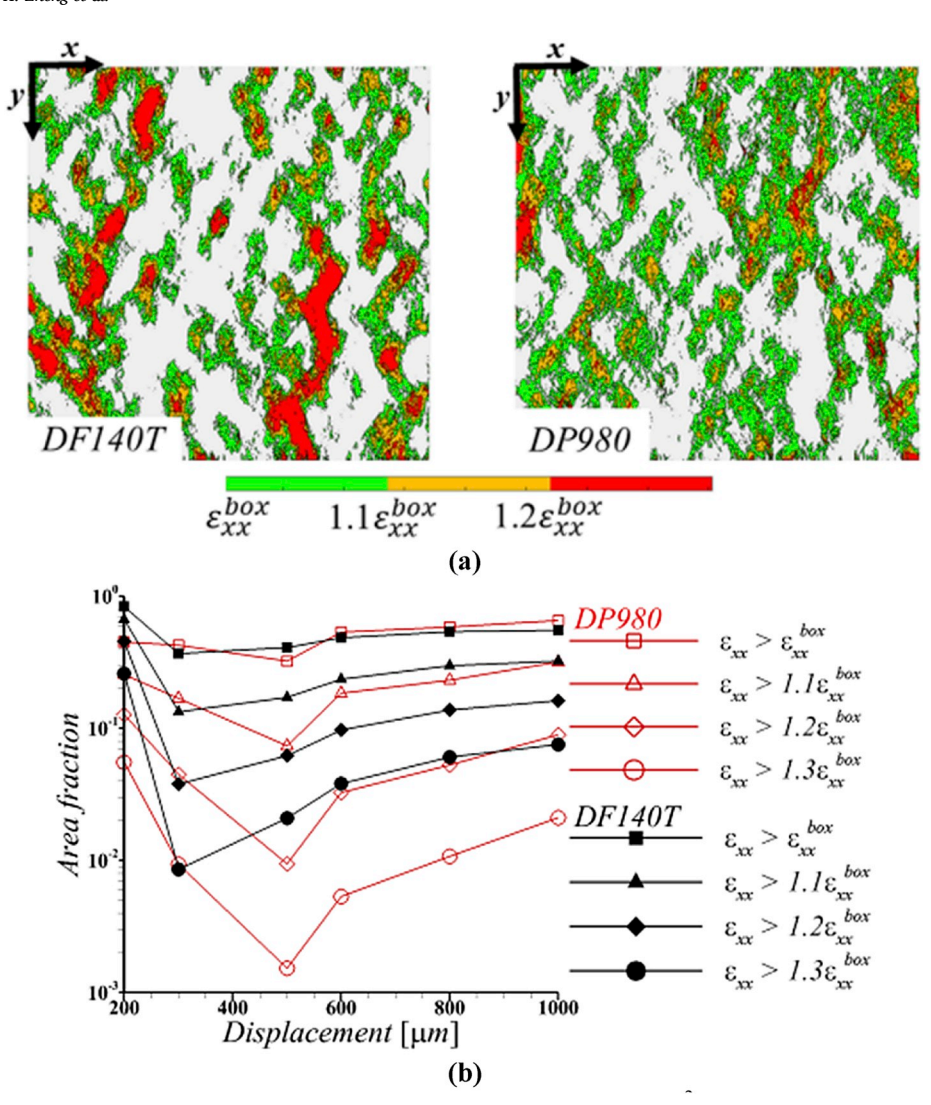


Fig. 3. (a) The distribution of the ε_{rr} strain in a 300by-300µm2 region in the center of the gauge section of the dog-bone tension specimen of DF140T and DP980 steels deformed to a (macroscale) displacement of 600 μ m. In (a) the values of ε_{xx} less than the value of ε_{xx} at the edges parallel to y-axis of the region of interest i.e. the 300-by-300 μ m² box, ε_{xx}^{box} , are white washed to highlight the regions of strain concentration. The tensile loading direction in (a) is along *x*-axis and the value of $\varepsilon_{xx}^{box} \approx 0.04$ for both the steels. (b) The evolution of the area fraction of various levels of ε_{xx} greater than the current value of ε_{rr}^{box} in the regions shown in (a) with imposed displacement on the dog-bone tension specimen of DF140T and DP980 steels. The y-axis in (b) is on logarithmic scale.

mechanical response of the dog-bone specimen of both the steels is very similar, at microscale the heterogeneous deformation is more pronounced in DF140T steel compared to DP980 steel. In the dog-bone specimen of DF140T steel, under imposed tensile loading along x-axis, ε_{xx} localizes in bands that are (roughly) oriented orthogonal to the loading direction even before the onset of maximum load.

The evolution of heterogeneous deformation, in particular, the extent of strain concentration at microscale in the dog-bone tension specimen of DF140T and DP980 steels is quantified in Fig. 3(b). Fig. 3(b) shows the evolution of the area fraction of various levels of ε_{xx} greater than the current value of ε_{xx}^{box} with imposed (macroscale) displacement. The results in Fig. 3(b) are only presented up to an imposed displacement of 1000 µm which is within the macroscopic uniform deformation regime, see Fig. 2(a). As shown in Fig. 3(b), at an imposed displacement of 200 μ m, the area fraction of all levels of strain concertation, $\varepsilon_{xx}/\varepsilon_{xx}^{box}$, is greater in DF140T steel compared to DP980 steel. With progressive deformation (increasing imposed displacement), the area fraction of all levels of $\varepsilon_{xx}/\varepsilon_{xx}^{box}$ first decreases due to the onset of plastic deformation in both ferrite and martensite phases and then tends to increase gradually in both the steels. At greater imposed displacements, the area fraction of low levels of $\varepsilon_{xx}/\varepsilon_{xx}^{box}$ is roughly the same in both the steels. However, the area fraction of $\varepsilon_{xx}/\varepsilon_{xx}^{box} > 1.2$ is greater in DF140T compared to DP980, highlighting the extremely heterogeneous deformation with regions of extremely high strain concertation in DF140T.

The distribution of the ε_{xx} strain in the reference configuration in a

500-by-250μm² region near the notch in the single-edge notch tension specimen of DF140T and DP980 steels deformed to a (macroscale) displacement of 200 µm is shown in Fig. 4(a). At the imposed displacement of 200 µm neither of the single-edge notch tension specimens have reached the maximum load. As shown in Fig. 2(b), the singleedge notch specimens of DF140T achieve an average maximum load of ~2092 N at an average extension of ~262 µm while those of DP980 achieve an average maximum load of ~2237 N at an average extension of \sim 330 μ m. In Fig. 4(a), the values of ε_{xx} less than the value of ε_{xx} at the edges parallel to the y-axis of the 500-by-250 μ m² box, ε_{xx}^{box} , are white washed to highlight the regions of strain concentration. As shown in the figure, in the single-edge notch tension specimen of both the steels, ε_{xx} localizes in wide bands originating from the corners of the deformed notch. Within this band the deformation is more heterogeneous with regions of greater strain concentrations for DF140T steel compared to DP980 steel. The difference between the deformation at microscale in the steels seen in Fig. 4(a) can be explained at least qualitatively based on the results shown in Fig. 3(a). Nevertheless, unlike the dog-bone specimen, the macroscale tensile response of the single-edge notch specimen of these steels differs significantly, see Fig. 2.

Similar to Fig. 3(b), the evolution of the extent of strain concentration at microscale in the single-edge notch tension specimen of both the steels is quantified in Fig. 4(b). The results in Fig. 4(b) are only presented up to an imposed displacement of 200 μ m which is before the onset of maximum load in Fig. 2(b). As shown in Fig. 4(b), at an imposed

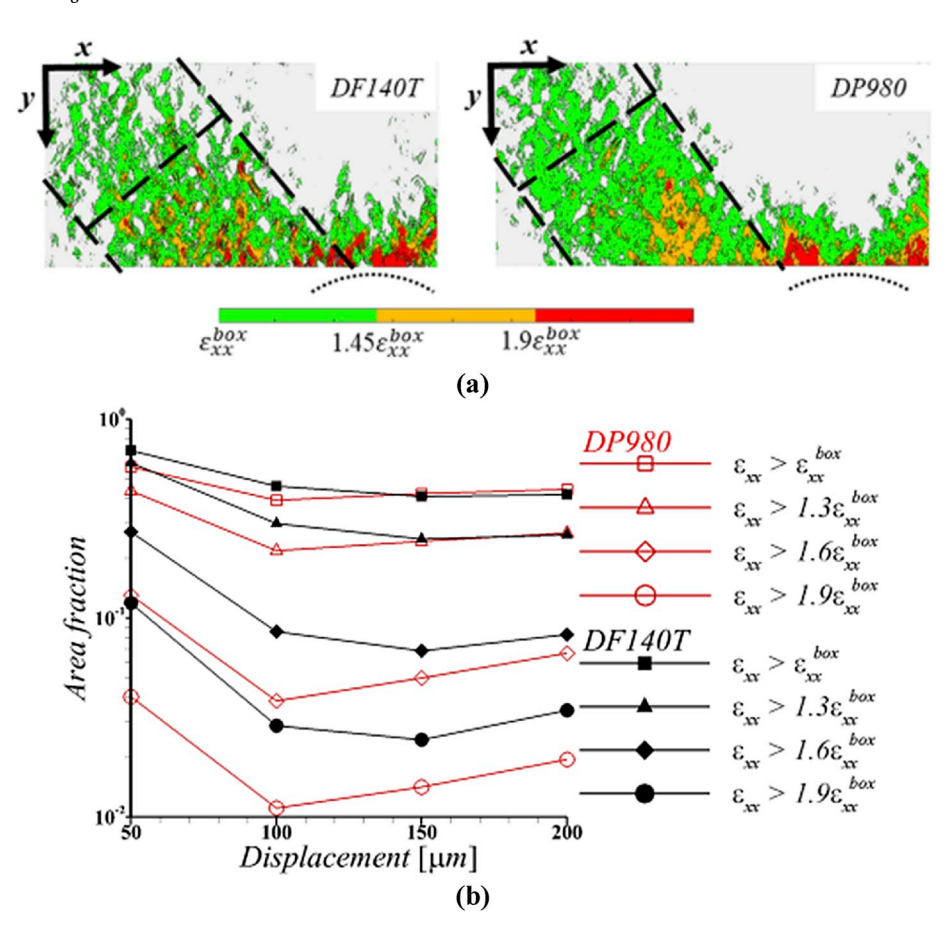


Fig. 4. (a) The distribution of the ε_{rr} strain in a 500by-250µm2 region near the notch in the single-edge notch tension specimen of DF140T and DP980 steels deformed to a (macroscale) displacement of 200 μ m. In (a) the values of ε_{xx} less than the value of ε_{xx} at the edges parallel to y-axis of the region of interest i.e. the 500-by-250 μ m² box, ε_{rr}^{box} , are white washed to highlight the regions of strain concentration. The tensile loading direction in (a) is along xaxis, the initial notch is along y-axis and the dotted arc marks the location of the notch tip. The value of $\varepsilon_{xx}^{box} \approx 0.052$ for DF140T steel and $\varepsilon_{xx}^{box} \approx 0.05$ for DP980 steel. **(b)** The evolution of the area fraction of various levels of ε_{xx} greater than the current value of ε_{rr}^{box} in the regions shown in (a) with imposed displacement on the single-edge notch tension specimen of DF140T and DP980 steels. The y-axis in (b) is on logarithmic scale.

displacement of 50 µm, the area fraction of all levels of strain concertation, $\varepsilon_{xx}/\varepsilon_{xx}^{box}$, is greater in DF140T steel compared to DP980 steel. With progressive deformation (increasing imposed displacement), the area fraction of all levels of $\varepsilon_{xx}/\varepsilon_{xx}^{box}$ first decreases and then tends to increase gradually in both the steels. At greater imposed displacements, the area fraction of low levels of $\varepsilon_{xx}/\varepsilon_{xx}^{box}$ is roughly the same in both the steels. However, the area fraction of $\varepsilon_{xx}/\varepsilon_{xx}^{box} > 1.6$ is greater in DF140T compared to DP980, highlighting the extremely heterogeneous deformation with regions of extremely high strain concertation in DF140T as shown in Fig. 4(a).

In a single-edge notch tension specimen, the regions near the free surface may exhibit greater shear-driven plastic deformation as the stress along the thickness direction approaches zero on the free surface of the specimen. Thus, it is imperative to analyze the extent of shear strain concentration at microscale in the single-edge notch specimen of

both the steels. The microscale distribution of in-plane shear strain, ε_{xy} , in the reference configuration in the single-edge notch tension specimen of both the steels in the same regions and at the same imposed displacement as in Fig. 4(a) is shown in Fig. 5. In both the steels, the positive values of ε_{xy} concentrate in triangular bands originating from the notch tip, while the values of ε_{xy} are negative on the left side of these triangular bands. The zero shear region between the two shear directions (positive and negative) is most susceptible to damage initiation. Similar to Fig. 4(a), in Fig. 5 as well, within the region of negative and positive values of ε_{xy} , the distribution of ε_{xy} is more heterogeneous with regions of greater strain concentrations in DF140T steel as compared to DP980 steel.

Figs. 3–5, show that at the same imposed (macroscopic) displacement the deformation at the microstructural length-scale is more heterogeneous with regions of greater strain concentrations in DF140T steel

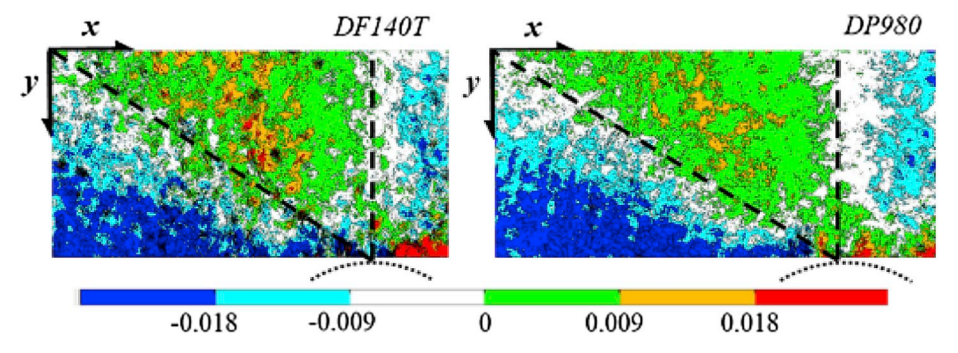


Fig. 5. The distribution of the $ε_{xy}$ strain in a 500-by-250μm² region near the notch in the single-edge notch tension specimen of DF140T and DP980 steels deformed to a (macroscale) displacement of 200 μm. The tensile loading direction is along *x*-axis, the initial notch is along y-axis and the dotted arc marks the location of the notch tip.

compared to DP980 steel in both the dog-bone and the single-edge notch tension specimens. To further quantify the extent of strain concentration or localization in the dog-bone and the single-edge notch tension specimens of the two steels, we now consider the variation of the area fraction of various levels of $\varepsilon_{xx}/\varepsilon_{xx}^{box}$ and ε_{xy} at a fixed imposed displacement, Fig. 6. As shown in Fig. 6, the area fraction of a given level of $\varepsilon_{xx}/\varepsilon_{xx}^{box}$ and ε_{xy} is in general greater in the single-edge notch specimen compared to the dog-bone specimen in both the steels. In the dog-bone specimen, the area fraction of both $\varepsilon_{xx}/\varepsilon_{xx}^{box}$ and ε_{xy} decreases with increasing values of $\varepsilon_{xx}/\varepsilon_{xx}^{box}$ and ε_{xy} , respectively, in both the steels. Also, the area fraction of a given level of $\varepsilon_{xx}/\varepsilon_{xx}^{box}$ and ε_{xy} is in general slightly greater in the dog-bone specimen of DF140T steel compared to that of DP980 steel. In the single-edge notch specimen of DP980 the area fraction of both $\varepsilon_{xx}/\varepsilon_{xx}^{box}$ and ε_{xy} also decreases with increasing values of $\varepsilon_{xx}/\varepsilon_{xx}^{box}$ and ε_{xy} , respectively. However, in the single-edge notch specimen of DF140T the area fraction of $\varepsilon_{xx}/\varepsilon_{xx}^{box}$ and ε_{xy} only decreases initially with increasing values of $\varepsilon_{xx}/\varepsilon_{xx}^{box}$ and ε_{xy} , respectively, and beyond a critical value of $\varepsilon_{xx}/\varepsilon_{xx}^{box}$ and ε_{xy} their area fraction tends to saturate, suggesting localization of both ε_{xx} and ε_{xy} .

3.3. Fracture characteristics

SE-SEM images of the fracture surface of the dog-bone tension specimen of DF140T and DP980 steels are shown in Fig. 7. The qualitative morphology of the fracture surface of the dog-bone tension specimen of both the steels is roughly the same. The fracture surface of both the steels exhibits a dimpled morphology indicative of ductile fracture due to nucleation, growth and coalescence of microscale voids. The fracture surface of both the steels at greater magnification shows large and deep holes together with relatively small dimples. The bimodal distribution of dimples on the fracture surface is characteristics of dual-phase materials undergoing elastic-plastic deformation in both the phases [7].

Fig. 8 shows SE-SEM images of the fracture surface of the single-edge notch tension specimen of DF140T and DP980 steels. The crack growth direction in the specimens of both the steels is marked with arrows in the left most low magnification image in Fig. 8(a) and (b), and the thickness of the flat specimens is along the vertical edges of the image. The low magnification image of the fracture surface of DF140T steel shows formation of shear lips near the free surfaces (horizontal edges of the image) of the specimen. For DF140T steel, the maximum reduction in

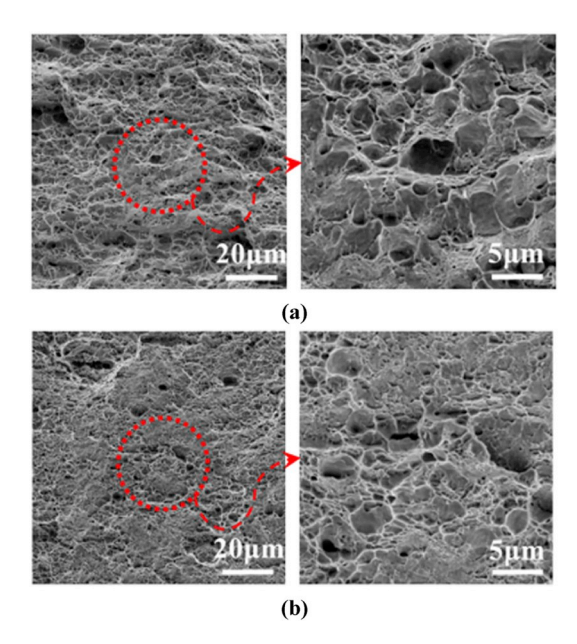
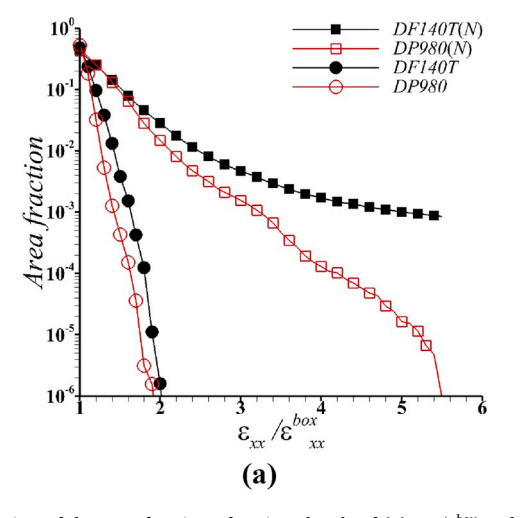


Fig. 7. SE-SEM images of the fracture surface showing the fracture morphologies of one-half of the flat dog-bone tension specimen of **(a)** DF140T and **(b)** DP980 dual-phase advanced high strength steels. The tensile loading direction is into the viewed plane. Magnified views of regions marked with dotted circles in left images are shown in right images.

the thickness of the fractured specimen (near the notch root) was found to be $\sim 9.8\%$ and the minimum reduction in the thickness of the fractured specimen (away from the notch root) was found to be $\sim 8.3\%$. On the contrary, the image taken at the same low magnification of the fracture surface of DP980 shows through thickness necking at the root of the deformed notch. For DP980 steel, the maximum reduction in the thickness of the fractured specimen (near the notch root) was found to be $\sim 23.3\%$ and the minimum reduction in the thickness of the fractured specimen (away from the notch root) was found to be $\sim 12.0\%$. This clearly shows that the single-edge notch specimen of DP980 steel first underwent through thickness necking which was then followed by damage evolution and crack initiation in center of the neck. However, in the single-edge notch specimen of DF140T steel a thumbnail shaped crack initiated along the thickness of the specimen without significant through thickness necking.



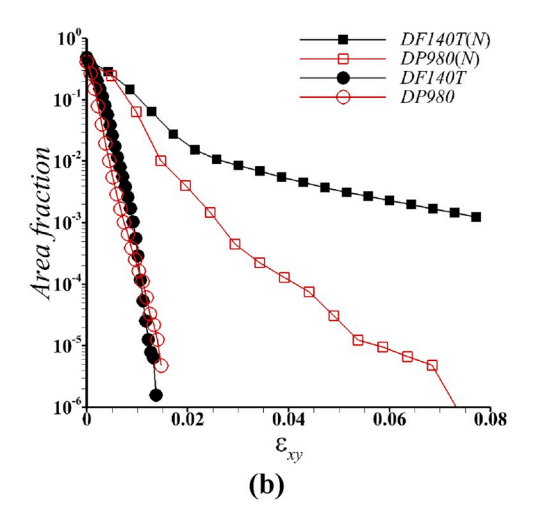


Fig. 6. The variation of the area fraction of various levels of (a) $ε_{xx}/ε_{xx}^{box}$ and (b) $ε_{xy}$ in a 300-by-300μm² region in the center of the gauge section of the dog-bone tension specimen and in a 500-by-250μm² region near the notch in the single-edge notch tension specimen (N) of DF140T and DP980 steels. For both the steels, the dog-bone tension specimen was deformed to a (macroscale) displacement of 600 μm and the single-edge notch tension specimen was deformed to a displacement of 200 μm. The y-axes in (a) and (b) are on logarithmic scale.

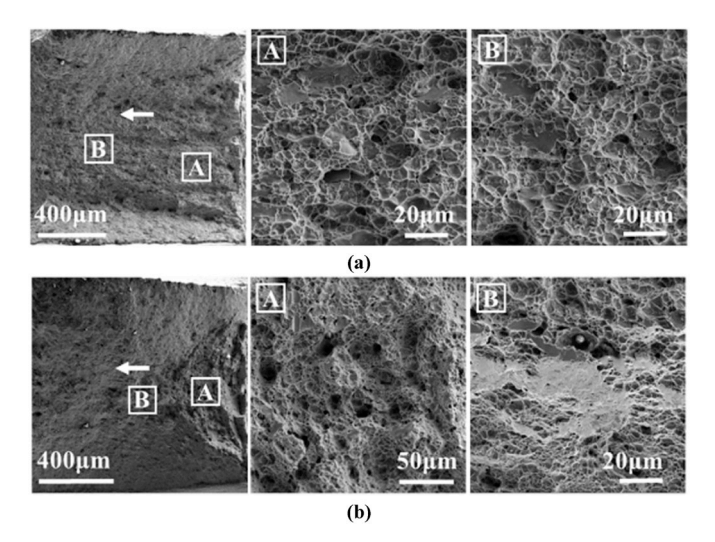


Fig. 8. SE-SEM images of the fracture surface showing the fracture morphologies of one-half of the flat single-edge notch tension specimen of **(a)** DF140T and **(b)** DP980 dual-phase advanced high strength steels. The tensile loading direction is into the viewed plane. Magnified views of regions marked as A and B in left most images are shown in center and right images, respectively.

The magnified images of the regions that are marked A near the notch root in the left most images in Fig. 8(a) and (b) show large and deep holes together with relatively small dimples in both the steels. In addition to dimples, for DF140T steel, the image labelled A in Fig. 8(a) also shows presence of depressions with sides resembling quasi-cleavage like planes suggesting pullout of hard precipitates from the relatively soft matrix. The magnified view of the fracture surface away from the notch root that is labelled B in Fig. 8(a) shows no change in the fracture surface morphology with progressive crack growth in the specimen of DF140T steel. However, the magnified view of the fracture surface away from the notch root in the specimen of DP980 steel, labelled B in Fig. 8 (b), is different from the fracture surface morphology near the notch root, see the image labelled A in Fig. 8(b). The fracture surface morphology away from the notch root in the specimen of DP980 steel contains relatively large quasi-cleavage like planes together with dimples. This is likely due to overload in the ligament post necking.

4. Discussion

Our experimental results show that despite significantly different nominal chemical composition and microstructure, the dog-bone tension specimens of DF140T and DP980 dual-phase steels exhibit very similar mechanical response. However, despite this, the mechanical response of the single-edge notch tension specimens of these two steels differs significantly. This is in contrast to any classical analysis that will predict the same mechanical response in the presence of a notch for two materials that have the same mechanical response under uniaxial tension. Furthermore, our microscale strain measurements, prior to the onset of maximum load (i.e. necking or fracture), show that irrespective of the similarities in the mechanical response of the dog-bone specimens and differences in the response of the single-edge notch specimens, the deformation at the microstructural length-scales in the two steels is always different. At the microstructural length-scale the deformation in both types of specimens of both the steels is always heterogeneous with the heterogeneous deformation being more pronounced in DF140T steel compared to DP980 steel. A quantitative analysis of the extent of strain concentration in both types of specimens of both the steels revealed that the single-edge notch specimen of DF140T steel exhibits in-plane localization of deformation. The in-plane localization of deformation in the single-edge notch specimen of DF140T steel results in onset of fracture without significant deformation along the out-of-plane (thickness) direction of the flat specimen. On the contrary, in the single-edge notch specimen of DP980 steel, onset of fracture occurs post out-of-plane necking near the notch root.

At the structural length-scale, in a dog-bone specimen, the stress state is uniaxial and the deformation is more or less uniform up until the onset of necking, whereas in a single-edge notch specimen, the stress state is quite complex and the deformation is always heterogeneous. Thus, it can be hypothesized that the interlacing of the heterogenous deformation at the structural and the microstructural length-scales leads to the in-plane localization of deformation in the single-edge notch specimens of DF140T steel. To proof this hypothesis, we carry out microstructure-based finite element analyses of the dog-bone and the single-edge notch tension specimens of both the steels. Schematic representations of the microstructure-based finite element models of the two-dimensional plane strain dog-bone and single-edge notch specimens of the two steels under consideration are shown in Fig. 9. In theory, it is possible to carry out microstructure-based finite element analyses of the full three-dimensional dog-bone and single-edge notch specimens. However, the finite element mesh density required to discretely model the micron-size microstructural features in the specimens of dimensions in millimeters will render the calculations prohibitively time consuming. Thus, for the dog-bone specimen, a two-dimensional slice of material with dimensions 500 μm along x-axis and 250 μm along y-axis is considered while for the single-edge notch specimen, half of the gauge section i.e. a slice of material with dimensions 2 mm along x-axis and 3 mm along y-axis with a notch of depth 1.5 mm along y-axis and tip radius 150 µm (located along the symmetry line OO', Fig. 9) is considered for numerical analyses.

The finite element calculations are carried out using the commercial finite element code ABAQUS/Standard [43]. To simulate the tension test of flat dog-bone specimen the $500\mu m \times 250\mu m$ slice of specimen is subjected to uniaxial velocity along x-axis on the two free edges parallel to y-axis, Fig. 9. To simulate the tension test of flat single-edge notch specimen, the one-half specimen, Fig. 9, is subjected to y-axis symmetry boundary conditions along OO' and uniaxial velocity along x-axis on the free edge parallel to y-axis. The finite element meshes use eight-node plane strain, CPE8R, elements of the ABAQUS/Standard element library [43]. The finite element mesh of $500\mu m \times 250\mu m$ slice of specimen contains 500×250 elements. The half single-edge notch specimen contains 400×400 elements in $400 \mu m \times 400 \mu m$ region close to the notch tip (marked as abcd in Fig. 9), and rather coarse mesh outside abcd. Next, to generate the discrete dual-phase microstructures in the finite element models, grayscale SEM images of microstructures of the two steels are superimposed on the finite element mesh and the material

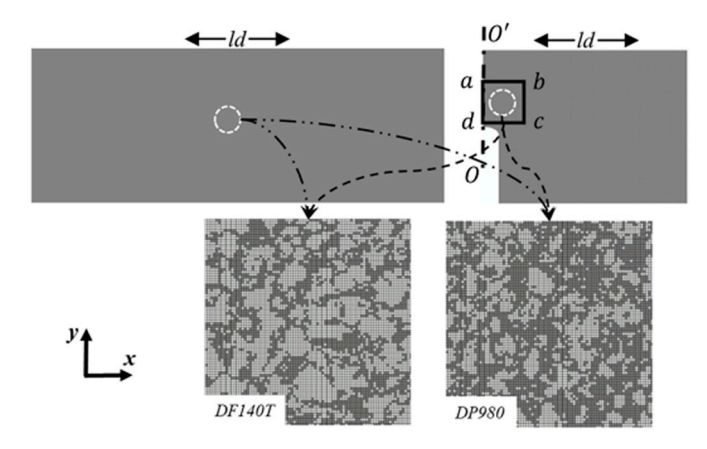


Fig. 9. Schematic showing a slice of defect free region of the gauge section of the dog-bone specimen and a slice of one-half of the single-edge notch specimen together with zoomed-in view of finite element mesh and superimposed dualphase microstructure of DF140T and DP980 dual-phase advanced high strength steels.

properties corresponding to respective microstructural features are assigned based on elements. In the $500\mu m \times 250\mu m$ slice of specimen, the dual-phase microstructures are discretely modeled throughout the specimen whereas, in the half single-edge notch specimen, the dual-phase microstructures are discretely modeled only in the region marked as abcd in Fig. 9. The region outside abcd in the half single-edge notch specimen is assigned the material properties corresponding to the overall (homogenized) mechanical response of the two steels under consideration.

In the microstructure-based finite element calculations, both ferrite and martensite phases and the overall (homogenized) dual-phase steels are modeled as rate-independent isotropic elastic-plastic material within finite strain J_2 flow theory. The Young's modulus and Poisson's ratio of both the phases and homogenized dual-phase steels are taken to be, 210 GPa and 0.3, respectively. The plastic response of both the phases and the homogenized dual-phase steels is modeled using the constitutive relation proposed in Ref. [6],

$$\sigma_e = \sigma_0 + k_1 \left(1 - \exp\left(-k_2 \varepsilon_e^p \right) \right) + h_s \left(\varepsilon_e^p \right)^n \tag{1}$$

where the first term marks the onset of plastic deformation in the soft ferrite phase, the second term represents the strong strain-hardening regime where the hard martensite phase largely remains elastic and the ferrite phase undergoes plastic deformation, and the third term represents the power-law strain-hardening regime in which both the phases undergo plastic deformation. Also, with the value of $k_1 = 0$, Eq. (1) reduces to simple Ludwik type constitutive relation that can be used to capture the stress-strain response of the constituent phases. The values of the constitutive parameters in Eq. (1) that best represent the plastic response of both the constituent phases (ferrite and martensite) of the two steels (DF140T and DP980) under consideration and their overall plastic response are obtained from the coupled micropillar compression test results of ref. [5] and representative volume element finite element calculations of refs. [6,7]. The final values of all the constitutive parameters for both the phases present in both the steels and for their overall plastic response are given in Table 1. The predicted nominal uniaxial stress-strain response of both the phases present in the two steels, and the predicted overall nominal uniaxial stress-strain response of the two steels using the constitutive parameters in Table 1 are shown in Fig. 10.

The key results of the microstructure-based finite element analyses of tensile tests of the dog-bone and the single-edge notch specimens of the two steels are shown in Fig. 11. Fig. 11 shows the variation of the predicted area fraction of various levels of $\varepsilon_{xx}/\varepsilon_{xx}^{box}$ and ε_{xy} in the dog-bone like and the single-edge notch specimens of the two steels at a fixed overall strain, ε_{xx}^{box} . The finite element results presented in Fig. 11 are qualitatively similar to the experimental results presented in Fig. 6. Similar to experimental results in Fig. 6, the numerical results in Fig. 11 show that: (i) for both the steels, the area fraction of a given level of $\varepsilon_{xx}/\varepsilon_{xx}^{box}$ and ε_{xy} is in general greater in the single-edge notch specimen compared to the dog-bone specimen; (ii) in both the specimens the area fraction of $\varepsilon_{xx}/\varepsilon_{xx}^{box}$ and ε_{xy} is in general greater in DF140T steel compared to DP980 steel; (iii) in dog-bone specimens, the area fraction

Table 1The values of the constitutive parameters in Eq. (1) that characterize the plastic response of both the phases (ferrite and martensite) and that of homogenized dual-phase, DF140T and DP980, advanced high strength steels.

	σ_0 (MPa)	k ₁ (MPa)	k ₂	h _s (MPa)	n
Ferrite (DF140T)	560.3	0	0	623.7	0.53
Martensite (DF140T)	1655.3	0	0	1628.2	0.39
Homogenized DF140T	430.0	367.9	464.8	1149.2	0.45
Ferrite (DP980)	542.5	0	0	3520.5	0.94
Martensite (DP980)	1072.7	0	0	688.2	0.45
Homogenized DP980	430.0	309.4	634.8	1222.6	0.44

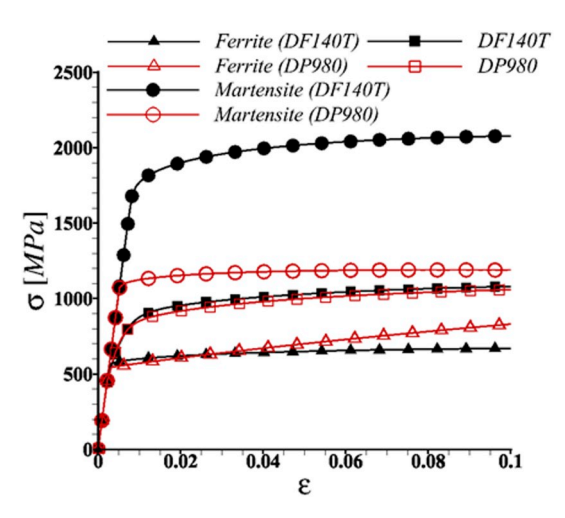


Fig. 10. Nominal stress (σ) – strain (ϵ) response of the ferrite and the martensite phases present in DF140T and DP980 dual-phase advanced high strength steels, and the overall nominal stress-strain response of DF140T and DP980 dual-phase advanced high strength steels predicted using the constitutive parameters given in Table 1.

of $\varepsilon_{xx}/\varepsilon_{xx}^{box}$ and ε_{xy} decreases with increasing values of $\varepsilon_{xx}/\varepsilon_{xx}^{box}$ and ε_{xy} , respectively, for both the steels; and (iv) in single-edge notch specimens, the area fraction of $\varepsilon_{xx}/\varepsilon_{xx}^{box}$ and ε_{xy} decreases with increasing values of $\varepsilon_{xx}/\varepsilon_{xx}^{box}$ and ε_{xy} , respectively, for DP980 steel but for DF140T steel, beyond a critical value of $\varepsilon_{xx}/\varepsilon_{xx}^{box}$ and ε_{xy} their area fraction tends to saturate. The results of the microstructure-based finite element analyses confirm that the interlacing of heterogeneous deformation at the structural and the microstructural length-scales can lead to localization of deformation in the single-edge notch specimens of DF140T steel.

The in-plane localization of deformation prior to the onset of maximum load (i.e. necking or fracture) in the single-edge notch specimen of DF140T steel, will affect the damage evolution and final failure. As shown in Fig. 12, in the single-edge notch specimen of DF140T steel the deformation predominantly localizes in the softer non strainhardening ferrite phase in bands emanating from the corners of the deformed notch. These bands are inclined at angles of $\sim 45^{\circ}$ and $\sim 135^{\circ}$ with respect to the loading axis. With progressive deformation, damage predominantly initiates and evolves in the ferrite phase within these bands and finally a crack nucleates along one of the bands resulting in premature fracture. However, due to a lack of in-plane localization of deformation, the single-edge notch specimen of DP980 steel undergoes through thickness necking near the notch root before fracture, Fig. 12. Therefore, in the single-edge notch specimen of DP980 steel, damage initiates and evolves in both the phases. In the absence of a dominant structural length-scale in the dog-bone specimens, both the steels undergo necking before fracture and exhibit the same mechanical response. The same mechanical response of the dog-bone specimens of the two steels is largely due to the competing effect of the overall microstructure and the microscale properties of the constituent phases. Recall that the microstructure of DF140T contains only $\sim\!39\,\pm\,2\%$ martensite compared to ${\sim}61\pm3\%$ martensite in DP980, and due to the differences in their nominal chemical composition, the strength of martensite of DF140T is greater than that of DP980 while the ferrite of DP980 exhibits slightly greater strain-hardening than that of DF140T.

In other words, the differences in the microstructure and the microscale properties always lead to significantly different deformation at the microstructural length-scale in the two dual-phase steels. Nonetheless, due to the imposed homogeneous deformation field at the structural length-scale in the dog-bone tension specimens, there is a separation between the structural and the microstructural length-scales. Therefore, the mechanical response of the dog-bone tension specimens of the two steels is effectively that of an unstructured homogenized

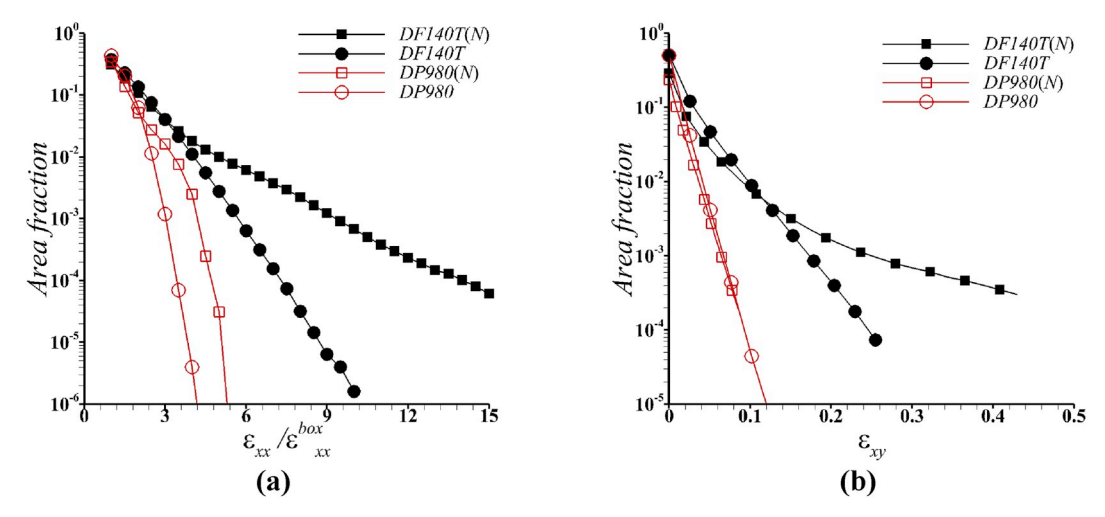


Fig. 11. The variation of the area fraction of various levels of (a) $\varepsilon_{xx}/\varepsilon_{xx}^{box}$ and (b) ε_{xy} in the defect free specimen (mimicking dog-bone specimen) and in the region marked as abcd in Fig. 9 near the notch in the single-edge notch tension specimen (N) of DF140T and DP980 steels. For both the steels, the defect free specimens were deformed to a macroscopic strain, $\varepsilon_{xx}^{box} = 0.04$, and single-edge notch tension specimens were deformed to an overall strain, $\varepsilon_{xx}^{box} = 0.05$, in the region marked as abcd in Fig. 9. The y-axes in (a) and (b) are on logarithmic scale.

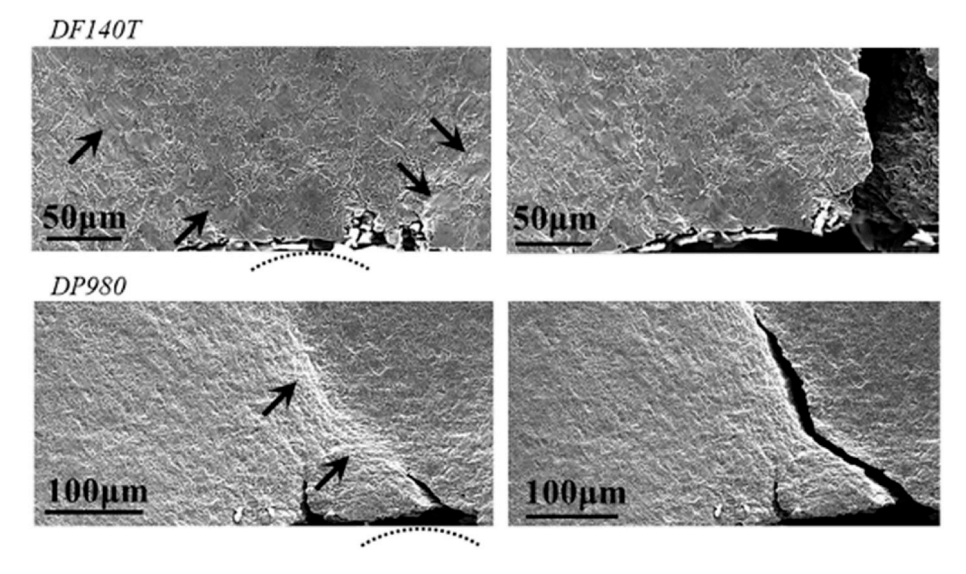


Fig. 12. SE-SEM images of surface microstructures near the notch in the single-edge notch tension specimen of DF140T and DP980 dual-phase advanced high strength steels, just before and after fracture. For DF140T, left and right images correspond to imposed macroscale displacements of 300 μm and 350 μm, respectively, while for DP980, left and right images correspond to imposed macroscale displacements of 500 μm and 515 μm, respectively.

material. However, the interlacing of the heterogenous deformation field at the structural and the microstructural length-scales in the single-edge notch specimens, results in extremely localized deformation in DF140T steel. The localized deformation in DF140T steel in turn results in breakdown in scale separation between the structural and the microstructural length-scales. Thus, the mechanical response of the single-edge notch tension specimens of dual-phase steels cannot be based on an unstructured continuum description of mechanical properties and must also involve the length-scales associated with the material microstructure.

5. Concluding remarks

We have elucidated how the interlacing of the structural and the microstructural length-scales affects the mechanical response of dual-phase steels. To this end, the mechanical response of the dog-bone and the single-edge notch specimens of two dual-phase steels, viz, DF140T and DP980, was characterized via in-situ SEM tensile tests. The

microstructure of DF140T steel contains ${\sim}39\pm2\%$ martensite compared to ${\sim}61\pm3\%$ martensite in DP980 steel. In addition, due to the differences in their nominal chemical composition, the strength of the martensite of DF140T steel is greater than that of DP980 steel while the ferrite of DP980 exhibits slightly greater strain-hardenability than that of DF140T. The results of in-situ tensile tests were complemented with microstructure-based digital image correlation, fractographic analysis and microstructure-based finite element analysis. The key conclusions of this work are as follows:

Despite significantly different microstructure and microscale properties, the dog-bone tension specimens of the two steels exhibit very similar mechanical response (yield strength, strain-hardening, ultimate tensile strength and ductility), but the mechanical response (maximum load bearing capacity and extension to failure) of the single-edge notch tension specimens of the two steels differs significantly.

- 2. At the microscale, even prior to the onset of maximum load (i.e. onset of necking or fracture), the deformation in both the dog-bone and the single-edge notch tension specimens of the two steels is always heterogeneous with the extent of heterogeneous deformation being more pronounced in DF140T steel compared to DP980 steel.
- 3. The interlacing of the heterogenous deformation at the structural and the microstructural length-scales in the single-edge notch tension specimens of DF140T steel results in localized deformation in the softer non strain-hardening ferrite phase. Thus, with further deformation damage predominantly initiates and evolves in the ferrite phase resulting in premature fracture.
- On the contrary, the single-edge notch tension specimens of DP980 steel undergo through thickness necking near the notch root before fracture.
- 5. The dog-bone tension specimens of both the steels undergo necking before fracture and their same mechanical response is due to the competing effect of the overall microstructure and the microscale properties of the constituent phases.

In summary, the most important message of this paper is that the characterization of mechanical response of a multiphase material is fundamentally different in a deformation field that is homogeneous, versus in a deformation field that is heterogeneous at the structural length-scale. In the former, the characterization of mechanical response can simply be based on an unstructured continuum description of the mechanical properties. However, the latter can lead to breakdown in structural-microstructural length-scale separation, which makes it extremely challenging to treat a multiphase material as an effective homogenized material. Thus, mechanistic analysis of multiphase materials in heterogeneous deformation fields at the structural length-scale, such as those observed in bending dominated manufacturing processes or near a structural discontinuity, should involve explicit consideration of the length-scales associated with the material microstructure. Here, we have only focused on elucidating the effect of the interlacing of the structural and the microstructural length-scales on the mechanical response of dual-phase steels under quasi-static loading conditions. The interlacing of these two length-scales will likely also be affected by other loading conditions, such as the imposed loading rate. We hope that our work will instigate further research in this direction.

Data availability

This article has no additional data. All experimental and numerical results are reproducible.

Declaration of competing interest

The authors declare that they have no known competing financial interests or personal relationships that could have appeared to influence the work reported in this paper.

CRediT authorship contribution statement

Xinzhu Zheng: Methodology, Validation, Investigation, Visualization, Formal analysis, Data curation, Writing - original draft. Hassan Ghassemi-Armaki: Resources, Validation, Writing - review & editing. Ankit Srivastava: Conceptualization, Methodology, Validation, Formal analysis, Data curation, Supervision, Funding acquisition, Writing - review & editing.

Acknowledgements

The dual-phase advanced high strength steels, DF140T and DP980, were kindly provided by the ArcelorMittal Global R&D, East Chicago, IN, USA. The finite element calculations reported on were carried out using high performance research computing resources provided by

Texas A&M University. The partial financial support provided by U.S. National Science Foundation grant CMMI - 1663130 are gratefully acknowledged.

References

- E8/E8M-16a. Standard Test Methods for Tension Testing of Metallic Materials, ASTM International, West Conshohocken, PA, 2016.
- [2] P. Bridgman, The stress distribution at the neck of a tension specimen, Transactions of the ASM 32 (1944) 553–574.
- [3] M. Rashid, Dual phase steels, Annu. Rev. Mater. Sci. 11 (1) (1981) 245-266.
- [4] R. Kuziak, R. Kawalla, S. Waengler, Advanced high strength steels for automotive industry, Archives of civil and mechanical engineering 8 (2) (2008) 103–117.
- [5] P. Chen, H. Ghassemi-Armaki, S. Kumar, A. Bower, S. Bhat, S. Sadagopan, Microscale-calibrated modeling of the deformation response of dual-phase steels, Acta Mater. 65 (2014) 133–149.
- [6] A. Srivastava, A.F. Bower, L.G. Hector, J.E. Carsley, L. Zhang, F. Abu-Farha, A multiscale approach to modeling formability of dual-phase steels, Model. Simul. Mater. Sci. Eng. 24 (2) (2016), 025011.
- [7] D. Gerbig, A. Srivastava, S. Osovski, L.G. Hector, A. Bower, Analysis and design of dual-phase steel microstructure for enhanced ductile fracture resistance, Int. J. Fract. 209 (1) (2018) 3–26.
- [8] W.J. Joost, Reducing vehicle weight and improving US energy efficiency using integrated computational materials engineering, JOM (J. Occup. Med.) 64 (9) (2012) 1032–1038.
- [9] R. Davies, Influence of martensite composition and content on the properties of dual phase steels, Metallurgical Transactions A 9 (5) (1978) 671–679.
- [10] L.F. Ramos, D.K. Matlock, G. Krauss, On the deformation behavior of dual-phase steels, Metallurgical Transactions A 10 (2) (1979) 259–261.
- [11] D.L. Steinbrunner, D.K. Matlock, G. Krauss, Void formation during tensile testing of dual phase steels, Metallurgical Transactions A 19 (3) (1988) 579–589.
- [12] J. Kang, Y. Ososkov, J.D. Embury, D.S. Wilkinson, Digital image correlation studies for microscopic strain distribution and damage in dual phase steels, Scr. Mater. 56 (11) (2007) 999–1002.
- [13] Y. Ososkov, D.S. Wilkinson, M. Jain, T. Simpson, In-situ measurement of local strain partitioning in a commercial dual-phase steel, Int. J. Mater. Res. 98 (8) (2007) 664–673.
- [14] G. Avramovic-Cingara, Y. Ososkov, M. Jain, D. Wilkinson, Effect of martensite distribution on damage behaviour in DP600 dual phase steels, Mater. Sci. Eng. A 516 (1–2) (2009) 7–16.
- [15] G. Avramovic-Cingara, C.A. Saleh, M. Jain, D. Wilkinson, Void nucleation and growth in dual-phase steel 600 during uniaxial tensile testing, Metall. Mater. Trans. A 40 (13) (2009) 3117.
- [16] K.S. Choi, W.N. Liu, X. Sun, M.A. Khaleel, Influence of martensite mechanical properties on failure mode and ductility of dual-phase steels, Metall. Mater. Trans. A 40 (4) (2009) 796–809.
- [17] X. Sun, K.S. Choi, W.N. Liu, M.A. Khaleel, Predicting failure modes and ductility of dual phase steels using plastic strain localization, Int. J. Plast. 25 (10) (2009) 1888–1909.
- [18] X. Sun, K.S. Choi, A. Soulami, W.N. Liu, M.A. Khaleel, On key factors influencing ductile fractures of dual phase (DP) steels, Mater. Sci. Eng. A 526 (1–2) (2009) 140–149.
- [19] H. Ghadbeigi, C. Pinna, S. Celotto, J. Yates, Local plastic strain evolution in a high strength dual-phase steel, Mater. Sci. Eng. A 527 (18–19) (2010) 5026–5032.
- [20] J. Kadkhodapour, A. Butz, S. Ziaei-Rad, S. Schmauder, A micro mechanical study on failure initiation of dual phase steels under tension using single crystal plasticity model, Int. J. Plast. 27 (7) (2011) 1103–1125.
- [21] S. Sodjit, V. Uthaisangsuk, Microstructure based prediction of strain hardening behavior of dual phase steels, Mater. Des. 41 (2012) 370–379.
- [22] S.-H. Choi, E.-Y. Kim, W. Woo, S. Han, J. Kwak, The effect of crystallographic orientation on the micromechanical deformation and failure behaviors of DP980 steel during uniaxial tension, Int. J. Plast. 45 (2013) 85–102.
- [23] R.S. Jamwal, A.M. Gokhale, S.P. Bhat, Quantitative fractographic analysis of variability in the tensile ductility of a high strength dual-phase steel, Metallogr. Microstruct. Anal. 2 (1) (2013) 30–34.
- [24] Q. Han, Y. Kang, P.D. Hodgson, N. Stanford, Quantitative measurement of strain partitioning and slip systems in a dual-phase steel, Scr. Mater. 69 (1) (2013) 13–16.
- [25] J. Marteau, H. Haddadi, S. Bouvier, Investigation of strain heterogeneities between grains in ferritic and ferritic-martensitic steels, Exp. Mech. 53 (3) (2013) 427–439.
- [26] C.C. Roth, D. Mohr, Effect of strain rate on ductile fracture initiation in advanced high strength steel sheets: experiments and modeling, Int. J. Plast. 56 (2014) 19–44.
- [27] C.C. Tasan, J.P.M. Hoefnagels, M. Diehl, D. Yan, F. Roters, D. Raabe, Strain localization and damage in dual phase steels investigated by coupled in-situ deformation experiments and crystal plasticity simulations, Int. J. Plast. 63 (2014) 198–210.
- [28] H. Ghassemi-Armaki, R. Maaß, S.P. Bhat, S. Sriram, J.R. Greer, K.S. Kumar, Deformation response of ferrite and martensite in a dual-phase steel, Acta Mater. 62 (2014) 197–211.
- [29] A. Alaie, J. Kadkhodapour, S. Ziaei Rad, M. Asadi Asadabad, S. Schmauder, Formation and coalescence of strain localized regions in ferrite phase of DP600 steels under uniaxial tensile deformation, Mater. Sci. Eng. A 623 (2015) 133–144.
- [30] S.J. Marcadet, D. Mohr, Effect of compression–tension loading reversal on the strain to fracture of dual phase steel sheets, Int. J. Plast. 72 (2015) 21–43.

- [31] D. Yan, C.C. Tasan, D. Raabe, High resolution in situ mapping of microstrain and microstructure evolution reveals damage resistance criteria in dual phase steels, Acta Mater. 96 (2015) 399–409.
- [32] C.C. Tasan, M. Diehl, D. Yan, M. Bechtold, F. Roters, L. Schemmann, C. Zheng, N. Peranio, D. Ponge, M. Koyama, K. Tsuzaki, D. Raabe, An overview of dual-phase steels: advances in microstructure-oriented processing and micromechanically guided design, Annu. Rev. Mater. Res. 45 (1) (2015) 391–431.
- [33] T. Matsuno, C. Teodosiu, D. Maeda, A. Uenishi, Mesoscale simulation of the early evolution of ductile fracture in dual-phase steels, Int. J. Plast. 74 (2015) 17–34.
- [34] Q. Lai, O. Bouaziz, M. Gouné, L. Brassart, M. Verdier, G. Parry, A. Perlade, Y. Bréchet, T. Pardoen, Damage and fracture of dual-phase steels: influence of martensite volume fraction, Mater. Sci. Eng. A 646 (2015) 322–331.
- [35] J. Zhou, A.M. Gokhale, A. Gurumurthy, S.P. Bhat, Realistic microstructural RVE-based simulations of stress-strain behavior of a dual-phase steel having high martensite volume fraction, Mater. Sci. Eng. A 630 (2015) 107–115.
- [36] Q. Lai, L. Brassart, O. Bouaziz, M. Gouné, M. Verdier, G. Parry, A. Perlade, Y. Bréchet, T. Pardoen, Influence of martensite volume fraction and hardness on

- the plastic behavior of dual-phase steels: experiments and micromechanical modeling, Int. J. Plast. 80 (2016) 187-203.
- [37] S. Huang, C. He, Y. Zhao, Microstructure-based RVE approach for stretch-bending of dual-phase steels, J. Mater. Eng. Perform. 25 (3) (2016) 966–976.
- [38] E.E. Aşık, E.S. Perdahcıoğlu, A.H. van den Boogaard, Microscopic investigation of damage mechanisms and anisotropic evolution of damage in DP600, Mater. Sci. Eng. A 739 (2019) 348–356.
- [39] Y. Liu, D. Fan, S.P. Bhat, A. Srivastava, Ductile fracture of dual-phase steel sheets under bending, Int. J. Plast. (2019).
- [40] R. Chuang, D. WenJiao, Z. WeiGang, Effects of ferrite grain characteristics on strain distribution of dual-phase steel, Mater. Res. Express 6 (1) (2019), 016539.
- [41] J. Blaber, B. Adair, A. Antoniou, Ncorr: open-source 2D digital image correlation matlab software, Exp. Mech. 55 (6) (2015) 1105–1122.
- [42] B. Pan, K. Li, W. Tong, Fast, robust and accurate digital image correlation calculation without redundant computations, Exp. Mech. 53 (7) (2013) 1277–1289.
- [43] Abaqus User's Manual Version 6.10, 2010. Providence, RI.